

Proton Charge Radius from Lepton Scattering

Weizhi Xiong^{1,†}, Chao Peng^{2,†}

¹ Shandong University, Qingdao, Shandong 266237, China; xiongwsdu.edu.cn

² Argonne National Laboratory, IL, USA; cpeng@anl.gov

† These authors contributed equally to this work.

Abstract: Protons are bound states of the strong interaction governed by Quantum Chromodynamics (QCD). Its charge radius (r_E^p) is an important quantity as it characterizes the spatial distribution of the proton's charge, which is carried by the quarks. On the other hand, the proton charge radius is an essential physical input for the bound-state Quantum Electrodynamics (QED) calculations for the hydrogen atomic energy levels. Nevertheless, the large discrepancy between r_E^p measurements from muonic hydrogen spectroscopy, and those from ep elastic scattering and ordinary hydrogen spectroscopy, have been puzzling physicists for over a decade. Tremendous efforts, in both theoretical and experimental sides, have been dedicated to providing various insights into this puzzle, yet certain issues still remain unresolved, particularly in the field of lepton scatterings. This review will focus on r_E^p measurements using lepton scatterings, the recent theoretical and experimental developments in this field, as well as future experiments using this technique.

Keywords: proton charge radius; proton electromagnetic form factor; lepton-proton elastic scattering;

1. Introduction

Protons, the most stable hadron in the visible universe, are bound states of the strong interaction governed by Quantum Chromodynamics (QCD), with quarks and gluons as the fundamental degrees of freedom. The root-mean-squared (rms) charge radius of the proton is an essential global quantity related to the spatial distribution of its charged constituents (the quarks) and characterizes the charge size of the proton. Theoretical calculations of this quantity from the first principle require precise knowledge of the proton's internal structure at the non-perturbative regime of QCD and are thus very challenging. The Lattice QCD, which has shown promising developments in the past decade, is expected to provide more precise *ab-initio* calculations of the proton charge radius in the near future that can be tested by the experimental results. On the other hand, the proton charge radius is an important physical input to the bound state Quantum Electrodynamics (QED) calculations for hydrogen atomic energy levels. It is highly correlated with the Rydberg constant (R_∞), which is one of the most precisely determined quantities in physics.

The proton charge radius can be determined from two well-established experimental methods [1]. The first method is to measure the proton electric form factor (G_E^p), which can be accessed through unpolarized electron-proton (ep) elastic scattering experiments [2–4], elastic scattering experiments utilizing polarization degrees of freedom [5–7], and e^+e^- annihilation experiments [8,9]. The rms charge radius is determined from the slope of G_E^p as the four-momentum transfer square Q^2 approaches 0:

$$\langle r_E^{p2} \rangle = -\frac{6}{G_E^p(0)} \left. \frac{dG_E^p(Q^2)}{dQ^2} \right|_{Q^2=0}, \quad (1)$$



Citation: Xiong, W.; Peng, C. Proton Charge Radius from Lepton Scattering. *Preprints* 2022, 1, 0. <https://doi.org/>

Publisher's Note: MDPI stays neutral with regard to jurisdictional claims in published maps and institutional affiliations.



Copyright: © 2022 by the authors. Licensee MDPI, Basel, Switzerland. This article is an open access article distributed under the terms and conditions of the Creative Commons Attribution (CC BY) license (<https://creativecommons.org/licenses/by/4.0/>).

where $G_E^p(0) = 1$ due to the charge normalization. Among these experimental results, high-precision low- Q^2 G_E^p data are dominated by those obtained from the unpolarized ep elastic scattering technique, which plays a critical role in the r_E^p extraction using this method.

The second method for the r_E^p measurement is hydrogen spectroscopy [10–16]. It exploits the fact that the proton has a finite size, which will shift the S-state energy levels. In other words, an S-state wave function of an electron is non-zero at the origin, and thus, it can move inside the proton and experience a “screening effect” due to the charge of the proton. The proton finite size effect can be quantified as [17]

$$\begin{aligned}\Delta E &= -4\pi\alpha G_E^p(0)|\psi_{n0}(0)|^2\delta_{l0} \\ &= 4\pi\alpha\frac{r_E^{p2}}{6}|\psi_{n0}(0)|^2\delta_{l0}.\end{aligned}\quad (2)$$

This effect slightly increases the electron energy level and is usually included in the Lamb shift. To measure r_E^p , one would need to measure at least one transition frequency between two different energy levels, with one of them being an S-state to include the proton finite size term. The proton charge radius is then extracted with all other terms precisely calculated within the framework of QED.

Before 2010, r_E^p values from modern ep elastic scattering and hydrogen spectroscopy experiments were generally consistent with each other [1]. Based on CODATA-2010 [18], the r_E^p amounts to 0.8758(77) fm and 0.895(18) fm from previous hydrogen spectroscopic and ep elastic scattering experiments, respectively. This agreement was strengthened in 2010 by the A1 collaboration at Mainz Microtron (MAMI), which extracted the proton charge radius using the unpolarized ep elastic scattering, giving $r_E^p = 0.8791(79)$ fm [2]. Based on the above-mentioned results, CODATA-2010 determined the recommended value of r_E^p as 0.8775(51) fm. Nevertheless, in the same year, the CREMA collaboration published a result using a novel muonic hydrogen (μH) spectroscopy method [10] and found that the extracted r_E^p was significantly different from the CODATA-2010 recommended value. In this experiment, a muonic hydrogen atom was produced by replacing the atomic electron of an ordinary hydrogen atom with a muon, which is about 200 times heavier. As a result, the Bohr radius is much smaller and the energy shift is more sensitive to the proton finite size effect. The r_E^p obtained from this μH measurement, 0.84184(67) fm, has an unprecedented 0.1% precision, but it is 4% or 7σ smaller than the CODATA-2010 recommended value, triggering the “proton charge radius puzzle”. Since then, a tremendous amount of effort, both theoretical and experimental, has been dedicated to understanding and resolving this discrepancy.

The largest theoretical uncertainty for the μH results lies in the contributions from Two-Photon Exchange (TPE) diagrams, which has been rigorously examined using many different approaches [19–24], and lately using Lattice QCD [25]. All these results are very consistent, and cannot explain the large discrepancy between the two r_E^p values. New models involving lepton-universality violation and new force carriers have been proposed [26–29], yet none of them has sufficient experimental evidence to be supported at the moment. The definition of r_E^p in spectroscopy and scattering experiments have been examined [17], and the two approaches are indeed measuring the same quantity. The r_E^p extraction from scattering experiments has long been a subject of active debate and has been extensively investigated [30–36], yet no consensus is reached on what the best approach is from the community. Promisingly, Lattice QCD has achieved significant progress over the last few years [37–44], reducing the uncertainty of r_E^p and starting to be impactful to the puzzle, yet more improvements are needed in order to reach a similar or better uncertainty compared to results from empirical fits on experimental G_E^p data.

On the experimental side, results from five ordinary hydrogen spectroscopic [12–16] have been published since the proton radius puzzle. The uncertainties of these new experiments are largely reduced thanks to many ground-breaking improvements, including laser techniques and careful control of various systematic uncertainties. Three of these new results [12,14,15] favor the μH values, including the most precise result by Grinin *et al.* [15], while one of them prefers the CODATA-2010 recommended value [18]. Interestingly, the latest ordinary hydrogen spectroscopic result by Brandt *et al.* [16], measuring the transition frequency between 2S-8D states, is about 3σ away from both the muonic results and the CODATA-2010 value, calling for more investigation and experiments from the spectroscopy community. For the lepton scattering side, the A1 collaboration at MAMI managed to reach a lower Q^2 of 0.0013 GeV² (nearly three times lower than the Mainz A1 2010 experiment), by using the technique of electron initial state radiation (ISR) [4]. The collaboration also performed another experiment exploiting a novel technique of a hydrogen gas jet target [45], which completely eliminates the backgrounds from target cell windows. Although the results from these two experiments were limited by various uncertainties and are not precise enough to strongly impact the puzzle, the development of these novel experimental techniques will certainly benefit future experiments. At the moment, the most impactful result from the unpolarized lepton scattering since the puzzle is from the PRad experiment [3] at Thomas Jefferson National Accelerator Facility (TJNAF, a.k.a. Jefferson Lab or JLab). Using a non-magnetic calorimetric setup with a windowless hydrogen-gas-flow target, and simultaneously measuring both elastic ep and Møller (ee) scatterings, the PRad experiment bears a set of systematic uncertainties different than the other modern scattering experiments. Its result, $r_E^p = 0.831(14)$ fm, favors the μH results. However, there is an obvious tension between the proton electric form factor data from PRad and those from the Mainz 2010 experiment, particularly in the Q^2 range between 0.01 GeV² and 0.06 GeV². This discrepancy becomes another puzzle that the scattering community needs to address in future experiments. The recent r_E^p measurements from both spectroscopy and electron scattering measurements are summarized in Fig. 1.

After over a decade, the proton charge radius puzzle still remains an unsettled issue in the field. The recent theoretical and experimental progress is promising to deepen our knowledge about this important integral quantity of the proton. This review focuses on the progress of the lepton scattering technique. We will first introduce the recent scattering experiments that were performed since the appearance of the proton charge radius puzzle, and then discuss the development on r_E^p calculation and extraction from form factor data. Lastly, we will discuss the remaining issues in the field, followed by a brief overview of the future lepton-proton elastic scattering experiments, that are either currently under preparation or taking data.

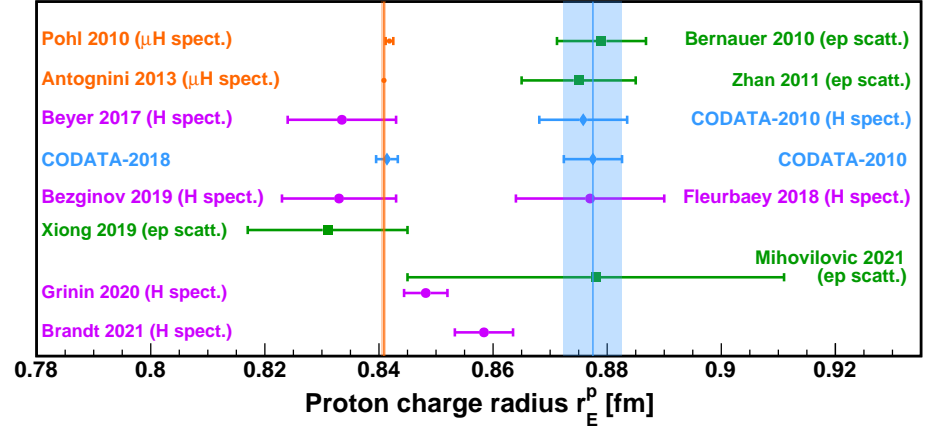


Figure 1. The proton charge radius determined from ep elastic scattering, hydrogen spectroscopic experiments, as well as world-data compilation from CODATA since 2010. The muonic spectroscopic measurements [10,11] are shown in orange dots, ordinary hydrogen spectroscopic results [12–16] are shown in purple dots, electron scattering measurements [2–5] are shown in green squares, and blue diamonds show the CODATA compilations [18,46].

2. Radius Extraction from Unpolarized Lepton-Proton Scattering Experiments

The unpolarized lepton-proton scattering technique is the commonly used experimental method for G_E^p measurements at low- Q^2 . Assuming the lepton mass can be neglected, the elastic scattering cross-section at Born level can be expressed by the Rosenbluth formula,

$$\frac{d\sigma}{d\Omega} = \left(\frac{d\sigma}{d\Omega} \right)_{\text{Mott}} \frac{1}{1 + \tau} \left[(G_E^p(Q^2))^2 + \frac{\tau}{\epsilon} (G_M^p(Q^2))^2 \right], \quad (3)$$

where $\tau = Q^2/(4M^2)$ and $\epsilon = [1 + 2(1 + \tau) \tan^2(\theta/2)]^{-1}$. Here M is the mass of a proton, and θ is the scattering angle of the lepton in the target rest frame. $(d\sigma/d\Omega)_{\text{Mott}}$ is the Mott cross-section, which describes the scattering off a structure-less and spin-less proton,

$$\left(\frac{d\sigma}{d\Omega} \right)_{\text{Mott}} = \frac{\alpha^2 \cos^2 \frac{\theta}{2} E'}{4E^2 \sin^4 \frac{\theta}{2} E}, \quad (4)$$

where α is the fine-structure constant, and E and E' are the energies of the incoming and outgoing lepton, respectively. In the case where the lepton mass m is not negligible, one can still use Eq. 3, with modifications to ϵ and Mott cross section as [47],

$$\epsilon = \left[1 - 2(1 + \tau) \frac{2m^2 - Q^2}{4EE' - Q^2} \right]^{-1}, \quad (5)$$

$$\left(\frac{d\sigma}{d\Omega} \right)_{\text{Mott}} = \frac{\alpha^2}{4E^2} \frac{1 - Q^2/(4EE')}{Q^4/(4EE')^2} \frac{E|\ell'|}{E'|\ell|} \frac{M(E'^2 - m^2)}{MEE' + m^2(E' - E - M)}, \quad (6)$$

where $|\ell|$ and $|\ell'|$ are respectively the three-momentum magnitudes of incident and scattered leptons.

In Eq. 3, G_E^p and G_M^p are respectively the proton electric and magnetic form factors and contain information regarding the spatial distribution of proton's charge and magnetization. They are linear combinations of the Dirac (F_1) and Pauli (F_2) form factors,

$$\begin{aligned} G_E^p(Q^2) &= F_1(Q^2) - \frac{Q^2}{4M^2} \kappa F_2(Q^2), \\ G_M^p(Q^2) &= F_1(Q^2) + \kappa F_2(Q^2), \end{aligned} \quad (7)$$

where κ is the proton anomalous magnetic moment.

Note that the cross-section (Eq. 3) contains contributions from both G_E^p and G_M^p at the same Q^2 . The Rosenbluth separation technique is often used to extract them from the cross-section. The first step is to rewrite Eq. 3 into a reduced form:

$$\left(\frac{d\sigma}{d\Omega}\right)_{\text{reduced}} = (1 + \tau) \frac{\epsilon}{\tau} \frac{\left(\frac{d\sigma}{d\Omega}\right)_{ep}}{\left(\frac{d\sigma}{d\Omega}\right)_{\text{Mott}}} = (G_M^p(Q^2))^2 + \frac{\epsilon}{\tau} (G_E^p(Q^2))^2. \quad (8)$$

If one measures the reduced cross-section at different ϵ but the same Q^2 , then G_E^p and G_M^p can be separately determined by the slope and intersection of a linear fit to the reduced cross-section data. Alternatively, one may extend this method by parameterizing G_E^p and G_M^p using different functions or models, and performing a direct fit to the unpolarized cross-section. This approach was used in the analysis of the Mainz 2010 experiment [2]. In addition, if the electric form factor is the only interesting observable, one may fix G_M^p with some models or parameterizations and extract G_E^p directly from the cross-section data. Such an approach is only applicable in the low- Q^2 and extreme-forward angular region. In such a case, the kinematic factor τ/ϵ will largely suppress the magnetic form factor contribution. This approach was used in the PRad experiment [3], for which the Q^2 coverage is $2.1 \times 10^{-4} < Q^2 < 5.8 \times 10^{-2} \text{ GeV}^2$ and the electron scattering angles between $0.7^\circ < \theta < 7.0^\circ$.

Once the form factors are extracted from the cross-section, one can obtain the radius from the slope of the form factor data at $Q^2 = 0$, as shown in Eq. 1. However, $Q^2 \rightarrow 0$ is not experimentally reachable, so the experiments need to use empirical fits or physics-based models to describe the form factor data measured at finite Q^2 , and then extrapolate to $Q^2 = 0$ for radius extraction. As a result, a systematic uncertainty associated with different choices of fitting functions or models is often inevitable. At the moment, there is no consensus in the community on what the best model or empirical fit is, and the choice is highly dependent on the kinematic range of the experiment. Nevertheless, one can suppress this systematic uncertainty by including high-precision form factor data with lower minimum Q_{min}^2 . And pseudo-data methods [33,34] that can test the robustness of different parameterizations and models also provide a valuable and effective handle on this uncertainty. Some popular empirical fits include, but are not limited to, the multi-parameter rational function of Q^2 (rational (N, M)),

$$G_E^p(Q^2) = \frac{1 + \sum_{i=1}^N p_i^a Q^{2i}}{1 + \sum_{j=1}^M p_j^b Q^{2j}}, \quad (9)$$

the multi-parameter polynomial expansion of Q^2 ,

$$G_E^p(Q^2) = 1 + \sum_{i=1}^N p_i Q^{2i}, \quad (10)$$

and the multi-parameter polynomial expansion of z :

$$G_E^p(Q^2) = 1 + \sum_{i=1}^N p_i z^i, \quad (11)$$

$$z = \frac{\sqrt{T_c + Q^2} - \sqrt{T_c - T_0}}{\sqrt{T_c + Q^2} + \sqrt{T_c - T_0}},$$

where $T_c = 4m_\pi^2$, m_π is the pion mass, and T_0 is a free parameter representing the point that is mapping onto $z = 0$. In addition, a simple dipole fitter is commonly used to flatten the G_E^p data over a large Q^2 range, as

$$G_E^p(Q^2) = \left(1 + \frac{Q^2}{p_1}\right)^{-2}. \quad (12)$$

With $p_1 = 0.71 \text{ GeV}^2$ it is referred to as the standard dipole form factor. From Eq. 9 to Eq. 12, the parameters p_i are the fitting parameters. In addition, fit to the experimental data often incorporates normalization uncertainties due to limited knowledge of absolute luminosity and limited Q^2 coverage from a single experimental setting. So a floating normalization parameter can be introduced as

$$f(Q^2) = n G_E^p(Q^2), \quad (13)$$

where f is the final functional form of the fitter, n is the floating normalization parameter, and $G_E^p(Q^2)$ can be, but not limited to, any of the functions from Eq. 9 to Eq. 12.

As mentioned earlier, r_E^p defined in Eq. 1 as the slope of G_E^p at $Q^2 = 0$ is responsible for the proton finite size term in hydrogen spectroscopy [17]. Nevertheless, the definition of proton charge radius as the second moment of the three-dimensional charge distribution of a proton does not contain the proper relativistic content [1,17]. To include the relativistic interpretation, One should instead, define a transverse charge density in the infinite-momentum frame [1,17,48,49],

$$\rho(b) = \frac{1}{2\pi} \int_0^\infty Q F_1(Q^2) J_0(Qb) dQ, \quad (14)$$

$$F_1(Q^2) = 2\pi \int_0^\infty b \rho(b) J_0(Qb) db, \quad (15)$$

where b is the impact parameter, and J_0 is the cylindrical Bessel function. If we expand $J_0(Qb)$, Eq. 15 can be expressed as

$$F_1(Q^2) \approx 1 - \frac{Q^2}{4} \langle b^2 \rangle + \frac{Q^4}{64} \langle b^4 \rangle - \dots, \quad (16)$$

where $\langle b^{2n} \rangle$ are the moments of the transverse charge density and are Lorentz invariant. The second moment or the root-mean-square transverse radius is then

$$\langle b^2 \rangle = 2\pi \int_0^\infty b^3 \rho(b) db. \quad (17)$$

If we take a Taylor expansion of $F_1(Q^2)$ at $Q^2 = 0$ and compare it to Eq. 16, we arrive at another definition of transverse radius,

$$\langle b^2 \rangle = -\frac{4}{F_1(0)} \left. \frac{dF_1(Q^2)}{dQ^2} \right|_{Q^2=0}. \quad (18)$$

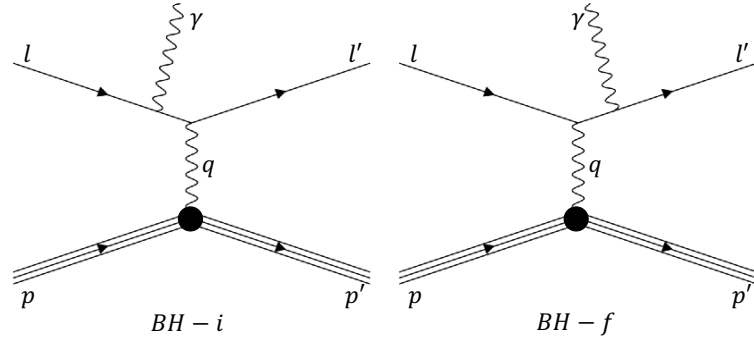


Figure 2. Feynman diagrams for the initial state (left panel, BH-i), and the final state (right panel, BH-f) Bethe-Heitler processes.

That is, the transverse radius is also related to the slope of F_1 at $Q^2 = 0$, similar to the proton charge radius definition Eq 1. Combining Eq 1, Eq. 18 and the derivative of Eq. 7 at $Q^2 = 0$, one arrives at a simple model-independent relation between $\langle b^2 \rangle$ and $\langle r_E^{p2} \rangle$:

$$\langle r_E^{p2} \rangle = \frac{3}{2} \left(\langle b^2 \rangle + \frac{\kappa}{M^2} \right). \quad (19)$$

This offers an alternative method to extract the proton charge radius r_E^p and was utilized in some recent analyses [48,49].

3. Recent Progress from Electron Scattering Experiments

In this section, we will briefly introduce the three unpolarized ep elastic scattering experiments performed after 2010. Two of these experiments, the initial-state radiation [4] and the jet-target experiment [45], were performed at MAMI, while the PRad experiment [3] took data at Jefferson Lab. The primary goal of these three experiments is to address the proton charge radius puzzle.

3.1. Initial-State Radiation Experiment at Mainz

The initial-state radiation (ISR) experiment at Mainz recently reported a reinterpretation of the existing elastic ep scattering data using the initial radiation technique [4]. The minimum Q^2 accessible to an elastic ep scattering experiment depends on the lowest beam energy and the most forward electron-scattering angle, often limited by the accelerator facility and experimental apparatus. This experiment further lowered the reachable Q^2 of the existing elastic ep cross-section data of Mainz down to $0.001 \text{ GeV}^2/c^2$ by determining the contribution from the initial-state Bethe-Heitler process (labeled as BH-i in Fig. 2) within the radiative tail of the elastic peak.

The Mainz ISR experiment measured the radiative tail in 2013 using the three spectrometer setup as the Mainz 2010 experiment. Three beam energies, $E_{beam} = 195, 330$ and 495 MeV , at the current between 10 nA and $1 \mu\text{A}$ were used with a 5-cm long liquid hydrogen target. The spectrometer B was adjusted to scan the full radiative tail at a scattering angle of 15.21° , while the spectrometer A was operated at a fixed setting to monitor the luminosity.

The measured radiative tail data were studied in conjunction with a dedicated Monte-Carlo simulation to separate the contributions from the diagram labeled as BH-i and as BH-f (see Figure 2). External radiative effects were corrected through the Mo and Tsai formalism [50], and the collisional loss was fit to a Landau distribution. The material thickness was determined by measuring the elastic electron scattering off residual nitrogen/oxygen gas with spectrometer A. As a result, a total of 25 data points within $0.001 \leq Q^2 \leq 0.017 \text{ GeV}^2/c^2$ were extracted

by the ISR technique. A polynomial fit with 21 free parameters including the normalization factors gives the proton charge radius of

$$r_E^p = 0.873 \pm 0.017_{\text{stat.}} \pm 0.059_{\text{syst.}} \pm 0.003_{\text{mod.}} \text{ fm}, \quad (20)$$

where the “mod” term stands for the uncertainty associated with higher moments in parameterizing the proton electric form factor. The collaboration also extracted the proton charge radius using an alternative approach, in which the data were compared with simulations based on a polynomial parameterization of the form factors, with the proton charge radius as the only free parameter. The data sets with beam energy $E_{\text{beam}} = 330$ and 495 MeV were used in this approach, while 195 MeV data were discarded due to the limited Q^2 coverage. The final result was given as a weighted average between the fits for the two energy settings:

$$r_E^p = 0.878 \pm 0.011_{\text{stat.}} \pm 0.031_{\text{syst.}} \pm 0.002_{\text{mod.}} \text{ fm}. \quad (21)$$

It is worth noting that the radii extracted from the two settings exhibit a 2.5σ tension between each other, with the higher energy setting favoring $r_p \approx 0.84$ fm and the other favoring $r_p \approx 1.0$ fm [4].

3.2. Proton Charge Radius Experiment at JLab

The Proton Charge Radius Experiment [3] at Jefferson Lab was performed in Hall B by the PRad collaboration in 2016. It measured the differential cross-sections of ep elastic scattering over a scattering angle from 0.7° to 7.0° at the beam energies of 1.101 GeV and 2.143 GeV. As shown in Figure 3, the PRad experiment exploited a calorimetric technique to measure the unpolarized ep elastic scattering, which, together with a novel windowless hydrogen-gas-flow target [51], provided a set of systematic uncertainties different from the other modern scattering experiments.

The PRad detector system consists of a Hybrid Calorimeter (HyCal) and a plane of Gas Electron Multipliers (GEM). It achieved relative energy resolutions of $2.4\%/\sqrt{E}$ (central PbWO_4 region) and $6.2\%/\sqrt{E}$ (outer Pb-Glass region) and a position resolution of $79 \mu\text{m}$ (single GEM plane) [52]. The system featured a large geometrical acceptance covering two orders of magnitude in Q^2 with one single beam energy setting, which significantly reduced the systematic uncertainties associated with the normalization factors for combining data from different experimental configurations.

The PRad target cell [51] was contained in a high-vacuum chamber connected to the beamline. A flow of cryogenic H_2 gas at $T_0 \approx 20$ K was consistently injected into the target cell, and then pumped out through the vacuum pumps attached to the target chamber. The Hydrogen gas was uniformly distributed along the four-centimeter-long cell, with a small fraction of the residual gas extending through the aperture at both ends of the target cell. An areal thickness greater than 2×10^{18} atoms/cm² was achieved for the PRad target. This windowless target removes a typical background source from scattering measurements – the target window, at the cost of additional background from the residual gas and difficulties in precisely determining the target thickness. The systematic uncertainties corresponding to the former were minimized by subtracting the data from empty target runs; those associated with the latter were suppressed by normalizing the elastic ep yield to that from the well-known Møller process.

Scattered electrons from both ep elastic and Møller scatterings were simultaneously measured during the PRad experiment. Within the kinematic coverage of this experiment, these two types of events could be easily separated by their energies. The experimental yields of ep elastic scattering were then normalized to those of the Møller process, and thus the luminosity is canceled at the first-order in this ratio measurement. In order to unfold the Born-level cross

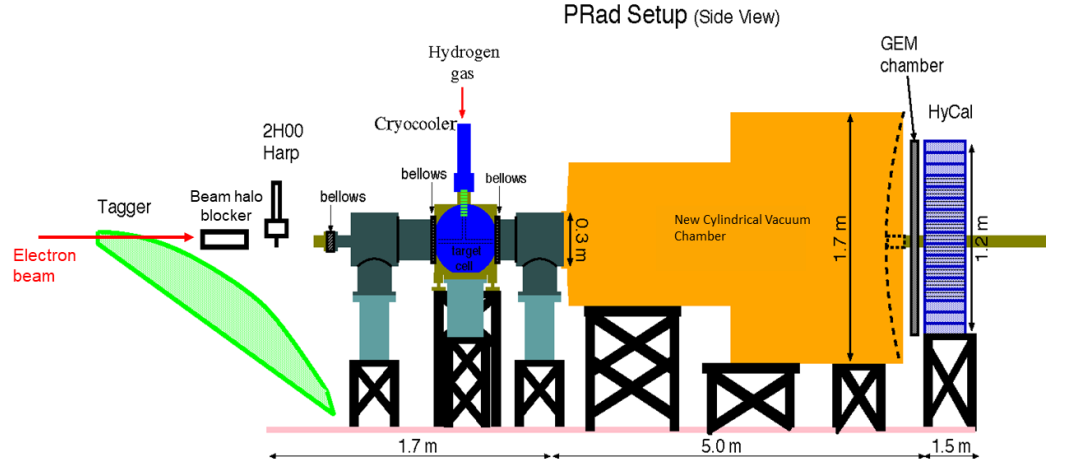


Figure 3. The schematic of the PRad experiment.

sections, an iterative process of radiative corrections based on a full GEANT4 [53] simulation and complete first-order calculations beyond the ultra-relativistic approximation (URA) [54] was applied to the data. The proton's electric form factors were eventually extracted with the Q^2 from $2.1 \times 10^{-4} \text{ GeV}^2$ to $5.8 \times 10^{-2} \text{ GeV}^2$. According to Eq. 8, the measured cross sections include the contributions from both electric and magnetic form factors, in which G_E^p is the predominant term at low Q^2 . In PRad case, the G_M^p contribution ranges from 0.015% to 0.06% for the lowest Q^2 data that is only achievable with the 1.1 GeV beam, and hence is negligible there. At higher Q^2 , G_M^p contribution was estimated by the Kelly parameterization [57] and its associated systematic uncertainty for the extracted G_E^p is less than 0.3%.

As a result, the PRad collaboration extracted the proton charge radius through a Rational (1, 1) (see Eq. 9) fit over the measured electric form factors, amounted to [3]

$$r_p = 0.831 \pm 0.007_{\text{stat}} \pm 0.012_{\text{syst}} \text{ fm.} \quad (22)$$

Its result favors the μH spectroscopy values from the CREMA collaboration [10,11]. Despite the fact that the systematic uncertainties of the PRad experiment are very different than those of the other modern scattering experiments, PRad value is in direct conflict with the proton charge radius extracted from the Mainz 2010 experiment [2] or the JLab recoil polarization experiment [5]. In addition, a data tension of G_E^p between PRad and Mainz A1 was observed, particularly in the range of $0.01 < Q^2/\text{GeV}^2 < 0.06$. These issues are discussed in details in Section 5.

3.3. Jet Target Experiment at Mainz

The Mainz jet-target experiment recently re-measured the proton electric form factor at low- Q^2 from 0.01 to 0.045 GeV^2 [45] and investigated the aforementioned data tension between PRad and Mainz A1. This experiment measured elastic ep scattering with a novel cryogenic supersonic gas jet target [55] at MAMI using the A1 multi-spectrometer facility.

The supersonic jet target deployed in this experiment was operated with molecular hydrogen gas cooled down to cryogenic temperatures at the A1 spectrometer with $E_{\text{beam}} = 315 \text{ MeV}$ and $I_{\text{beam}} = 20 \mu\text{A}$. In contrast to the gas-flow target used by PRad, this target was designed to have a compact length of about 1 mm and to achieve a comparable areal thickness of $10^{18} \text{ atoms/cm}^2$ at a nominal gas-flow rate $q_V = 2400 l_n/h$ and temperature $T_0 = 40 \text{ K}$. The

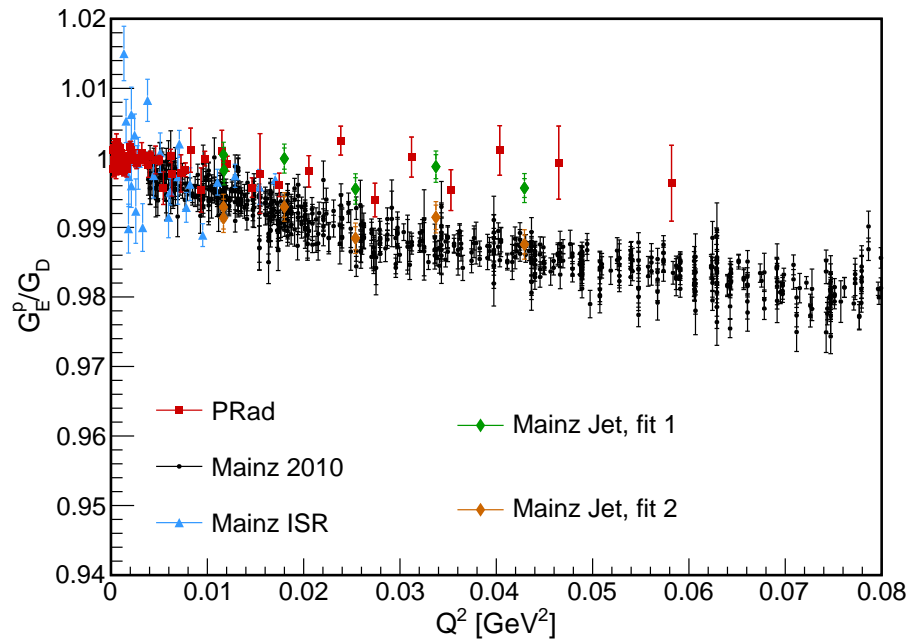


Figure 4. The proton electric form factor measured in the Mainz jet target experiment. The global luminosity was fit to PRad (Mainz jet, fit 1) and Mainz A1 (Mainz jet, fit 2) separately. Also shown are the G_E^p data, normalized by the standard dipole form factor, from the Mainz ISR [4], PRad [3], and the Mainz 2010 [2] experiments.

target system was contained in a high-vacuum scattering chamber, where the cryogenic gas was compressed through a vertical convergent-divergent nozzle and then formed jets that interacted with the horizontally traversing electron beam at a certain angle. The jets were eventually disposed into an aligned catcher placed a few mm away. A veto system, including a pair of tungsten collimators and a double-arm scintillating detector, was mounted upstream of the target to reject the background from the beam halo hitting the nozzle-catcher structure.

The experiment collected elastic ep scattering data with scattering angles from 15° to 40° , reaching a low Q^2 down to 0.01 GeV^2 . Beam-halo-associated backgrounds were significantly removed by the collimators; but the veto detectors didn't survive under the operating circumstances, leaving some backgrounds from the halo. The background was further studied with a low flow-rate run at $q_V = 50 l_n/h$ since a zero flow-rate run is not technically feasible. The collected data went through a radiative correction process based on simulation with a re-developed generator adapted from the OLYMPUS experiment [56]. The experiment cannot measure the absolute luminosity because the density distribution of the target that overlaps with the beam is not directly measurable. Thus, the ep scattering at 30° served as a luminosity monitor in the experiment, and the global normalization of the luminosity was set to be a free parameter for fit.

Figure 4 shows the measured G_E^p from this experiment, with the G_M^p contribution estimated by Kelly's parameterization [57]. The global luminosity was fit to PRad's rational (1,1) and Mainz's polynomial parameterizations for the G_E^p separately. The jet-target experimental data fits are consistent with both PRad and Mainz parameterizations, with a slightly better χ^2 from PRad's rational (1,1) fit. Due to the limited statistical uncertainty, the experiment is not able to resolve the data tension between PRad and Mainz at $0.01 < Q^2/\text{GeV}^2 < 0.06$. However, this experiment proves the feasibility of deploying a windowless jet target with high-resolution spectrometers, it also provides a set of systematic uncertainties very different from the previous

spectrometer experiments with a traditional target. The technique used in this experiment will certainly benefit certain future experiments, *e. g.*, the MAGIX experiment at MESA [55].

4. Recent Re-Analyses and Lattice QCD Calculations

In parallel with the recent experimental progress, re-analyses of world form factor data and Lattice QCD calculations continue to be an active research field. They are able to provide very unique insights into the proton charge radius puzzle. In this chapter, we will review the recent developments from these two categories. Some of the earlier studies are discussed in the review by Gao and Vanderhaeghen [1].

4.1. Re-analysis of Form Factor Data

In this subsection, we focus on the recent re-analyses of the world data after the PRad experiment. These studies can be categorized into two types: radius extraction based on physics-driven models, and from empirical fits or statistical methods. A compilation of proton charge radius from some of these recent studies is shown in Fig. 5.

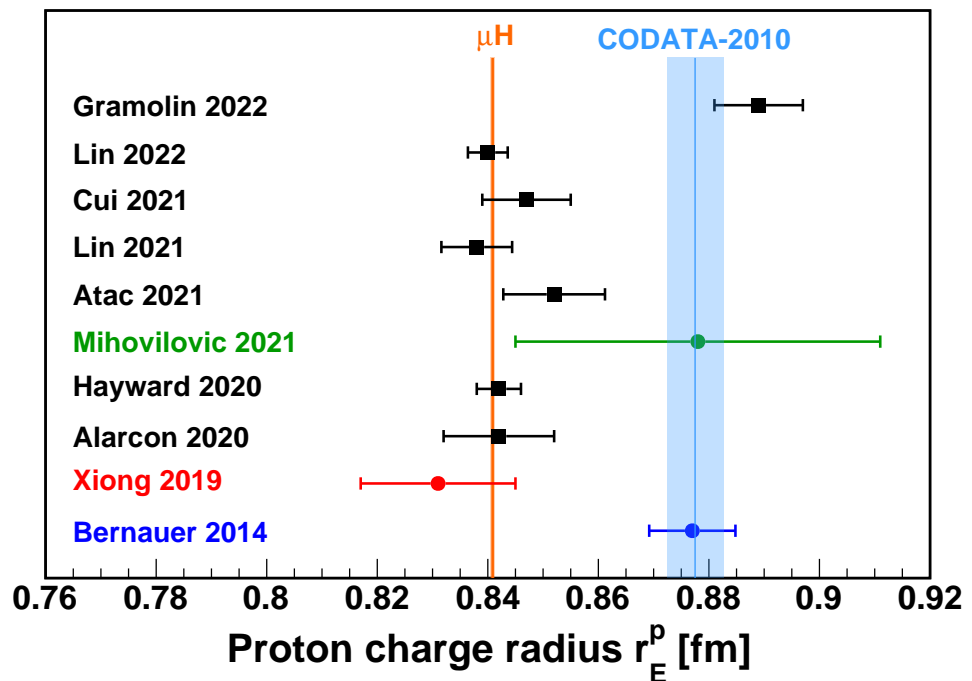


Figure 5. The proton charge radius extracted from a number of recent re-analyses [8,35,36,48,49,58,59] (black squares), as well as those from the original analyses of three recent unpolarized ep elastic scattering experiments (colored dots). The dark blue dot is for the Mainz 2010 experiment [2,60], the red dot is for the PRad experiment [3], and the dark green dot is for the Mainz ISR experiment [4]. The orange line and band correspond to the 2013 μ H spectroscopic measurement [11], and the light blue line and band correspond to the CODATA-2010 recommended value [18].

Alarcón, Higinbotham and Weiss [35] developed a novel and state-of-the-art theoretical framework, combining dispersion analysis and chiral effective field theory (DI χ EFT). In this model, the electromagnetic form factors are related to the dispersion integral of the spectral function over $t \equiv -Q^2$. With each input value of charge and magnetic radius, the model can generate a unique set of G_E^p and G_M^p up to $Q^2 \sim 1 \text{ GeV}^2$ with a well-controlled theoretical uncertainty. This model was applied to fit the Mainz 2010 cross-section data set [2,60], with

the proton charge and magnetic radii as free parameters. Floating normalization parameters were also included in the fit, similar to what was done in the original Mainz analysis [2,60]. Particularly, since the DI χ EFT model can predict the Q^2 -dependency of G_E^p and G_M^p given the electromagnetic radii, the model naturally avoids the uncertainties in these floating parameters due to different choices of empirical fitters. Applying this model to the Mainz data with Q^2 up to 0.5 GeV^2 gives:

$$\begin{aligned} r_E^p &= 0.842 \pm 0.002_{\text{fit}} \pm 0.010_{\text{theory}} \text{ fm}, \\ r_M^p &= 0.850 \pm 0.001_{\text{fit}} \pm 0.010_{\text{theory}} \text{ fm}, \end{aligned} \quad (23)$$

with a reduced χ^2 of 1.39. Extending the Q_{max}^2 to 1 GeV^2 for the same data set, using a rebinned version of the Mainz data [30], or including also the PRad data all produce very similar results, which show the stability and robustness of the extraction.

Lin, Hammer and Meißner have done a series of studies, applying the dispersion theory to world data from space-like measurements (unpolarized and polarized e - p elastic scattering) [59, 61], and lately, extending the study to include time-like measurements (e^+e^- annihilation and reverse process) as well [8]. Combining both space-like and time-like measurements, their final result on proton electromagnetic radii are [8]

$$\begin{aligned} r_E^p &= 0.840_{-0.002-0.002}^{+0.003+0.002} \text{ fm}, \\ r_M^p &= 0.849_{-0.003-0.004}^{+0.003+0.001} \text{ fm}, \end{aligned} \quad (24)$$

where the first errors are statistical and the second errors are systematic uncertainties. In addition, they also manage to determine the Zemach radius and the third Zemach moment, both of which are consistent with Lamb shift and hyper-fine splittings in μH measurement [11].

Gramolin and Russell [49] exploited an alternative r_E^p extraction method that does not rely on getting the slope of G_E^p at $Q^2 = 0$. As discussed in Ch. 2, this two-dimensional transverse charge density has a well-defined relativistic interpolation and can be related to the Dirac form factor ($F_1(Q^2)$) through a two-dimensional Fourier transform (Eq. 14). For the second moment of the transverse charge density $\langle b^2 \rangle$, one may extract it from the slope of F_1 at $Q^2 = 0$ as shown in Eq. 18, or one can explore the definition of the second moment (Eq. 17), once a parameterization of $F_1(Q^2)$ is obtained at all values of Q^2 . The latter approach gives a larger emphasis on data points at higher Q^2 . The proton charge radius r_E^p can then be obtained from $\langle b^2 \rangle$, based on the model-independent relation Eq. 19. The authors applied the latter approach to the cross-section measurements from the Mainz 2010 experiment [2] and extracted both Dirac and Pauli form factors. The proton charge radius determined in this analysis is

$$r_E^p = 0.889(5)_{\text{stat.}}(5)_{\text{syst.}}(4)_{\text{model}} \text{ fm}, \quad (25)$$

which is consistent with the original Mainz 2010 results [2,60].

On the other hand, Atac *et al.* [48] also took a similar route, exploiting the nucleon transverse density and the Dirac form factor. In this study, a flavor decomposition was performed for the Dirac form factor F_1 assuming isospin symmetry, and both proton and neutron form factor world data were included. To obtain the transverse charge radius of different quark flavors, a variety of functional forms were applied to fit the data in order to obtain the form factor slope at $Q^2 = 0$. After that, the proton charge radius can be determined from Eq. 19. The final result of this study is,

$$r_E^p = 0.852 \pm 0.002_{\text{stat.}} \pm 0.009_{\text{syst.}} \text{ fm}. \quad (26)$$

Excluding the PRad data gives almost the same result but with slightly larger uncertainties, amounting to 0.857(13) fm. This study also reported the first extraction of neutron charge radius based on form factor data: $\langle r_E^{n^2} \rangle = -0.122 \pm 0.004_{\text{stat.}} \pm 0.010_{\text{sys.}} \text{ fm}^2$.

Meanwhile, charge radius extraction from empirical fits and statistical methods remains an active subject in the research field. Hayward and Griffioen [58] extracted both proton and deuteron charge radii, by applying a variety of empirical fits to the low- Q^2 ep and ed scattering world data prior to and including the Mainz 2010 data set [2]. The authors examined possible over- and under-estimation of point-to-point uncertainties in these data set, and developed a comprehensive algorithm to study possible systematic biases due to different fit functions. They also minimized the total uncertainty by choosing the optimal value of maximum Q^2 for the fitted data set. The extracted r_E^p is 0.842(4) fm, dominated by the Mainz 2010 data set. Barcus, Higinbotham, and McClellan [62] re-analyzed the Mainz 2010 data set, using a similar polynomial expansion (Eq. 10) as in the Mainz 2010 original analysis [2,60]. The authors could reproduce the Mainz results quite well when using an unbounded polynomial fit, similar to what was done in the original analysis. However, one can obtain a much smaller r_E^p (0.854 fm) once an additional constraint is applied to the fitting parameters. That is, fitting parameters in the polynomial must have successively alternating signs, which would make the polynomial approximately completely monotonic. Zhou *et al.* [63] attempted to offer a possible explanation for the G_E^p discrepancy between the PRad and the Mainz 2010 data sets, particularly in the Q^2 range between 0.01 GeV² to 0.06 GeV². The authors first noticed that the Rational (1, 1) functional form (see Eq. 9) is able to provide an excellent approximation to the state-of-the-art DI χ EFT model [35]. And then, both G_E^p and G_M^p were parameterized by the Rational (1, 1) functions, and were fitted simultaneously to the Mainz 2010 cross-section data up to $Q^2 = 0.5 \text{ GeV}^2$. The large discrepancy between the PRad and Mainz 2010 G_E^p data was found to be mostly removed following this approach.

Other than traditional empirical fits, Cui, Binosi, Roberts and Schmidt [36] took an innovative approach, by using the statistical Schlessinger Point Method (SPM) to extract the proton charge radius. Unlike traditional empirical fits, the method does not rely on a particular functional form, and the local and global features of the underlying curve are captured by a set of continuous fraction interpolations. Applying this method to the PRad data yields $r_E^p = 0.838 \pm 0.005_{\text{stat.}} \text{ fm}$, where the statistical uncertainty was estimated using the bootstrap method. When applying to the Mainz 2010 data set with $3.8 \times 10^{-3} < Q^2/\text{GeV}^2 < 1.4 \times 10^{-2}$, the result is $r_E^p = 0.856 \pm 0.014_{\text{stat.}} \text{ fm}$. Including all data from Mainz 2010 experiment yields almost the same central value but with slightly larger statistical uncertainty. Combining the two data sets, the final result is

$$r_E^p = 0.847 \pm 0.008_{\text{stat.}} \text{ fm.} \quad (27)$$

The SPM method was later also applied to the Mainz 2010 data set to extract the proton magnetic radius [64], and found that $r_M^p = 0.817 \pm 0.027_{\text{stat.}} \text{ fm}$.

4.2. Progress from Lattice QCD

Lattice QCD has proven to be a powerful tool to provide *ab-initio* calculations of various hadronic observables, including nucleon charge, spin, parton distribution functions, and so on [65–67]. Since the proton charge radius puzzle, the low Q^2 nucleon form factor and the proton charge radius have also drawn a tremendous amount of attention from the Lattice QCD community [68]. Typically, one would need to calculate the isovector ($G^v \equiv G^{u-d}$) and isoscalar ($G^s \equiv G^{u+d}$) nucleon form factors, which are respectively related to the difference and sum of the proton and neutron form factors. For the isovector form factors, only the connected diagrams need to be considered, while for the isoscalar form factors, in principle the

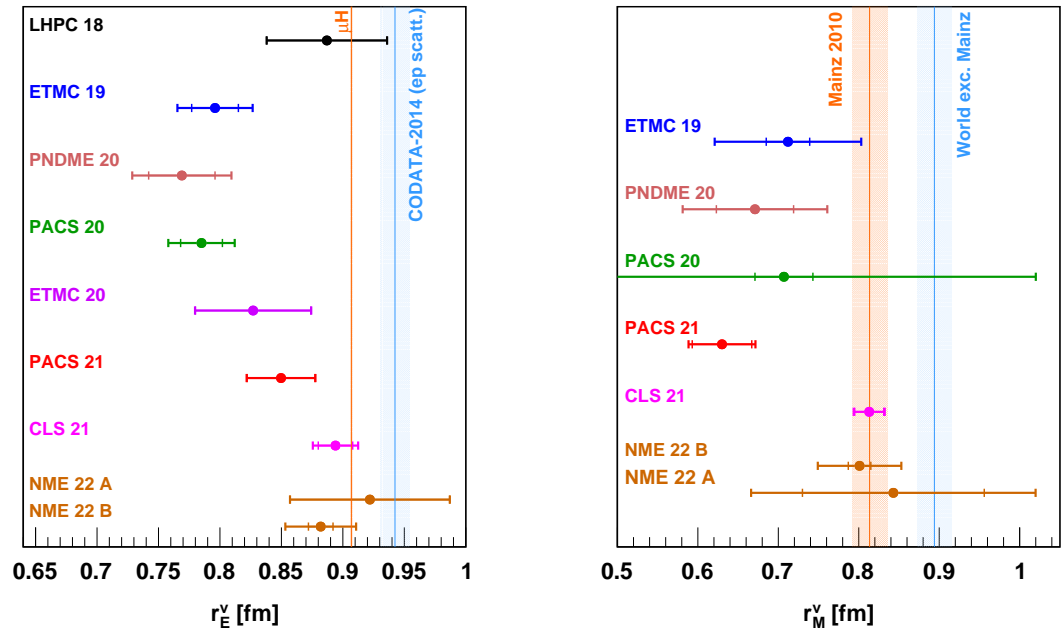


Figure 6. **Left panel:** the isovector charge radius from recent Lattice QCD calculations [37–44]. The vertical line and band in orange color are obtained based on the r_E^p result from the muonic hydrogen spectroscopic experiment [11], and the blue vertical line and band are obtained based on the CODATA-2014 r_E^p compilation [69]. Information about the neutron charge radius is obtained from PDG [70]. **Right panel:** the isovector magnetic radius from recent Lattice QCD calculations. The vertical line and band in orange color are obtained based on the r_M^p result from Lee *et al.* [30] for the Mainz 2010 data set, and the blue line and band are obtained based on the result from the same analysis, for the world data excluding the Mainz 2010 data set. Information about the neutron magnetic radius is obtained from PDG [70].

much more complicated and computationally more expensive disconnected diagrams have to be dealt with. The nucleon electromagnetic form factors are a linear combination of the isovector and isoscalar form factors. The isovector and isoscalar radii can also be extracted by taking the corresponding form factor slope at $Q^2 = 0$, similar to Eq. 1. In many cases, one needs to perform a fit to the lattice data using empirical fitters such as the dipole form (Eq. 12) and the z-transformation (Eq. 11), analogous to how the proton charge radius is extracted from experimental form factor data. In recent years, other methods have been developed to implement derivatives on the correlator level and are thus able to directly compute the form factor slope or nucleon radii [37,41,42]. Such approaches will avoid any systematic biases associated with form factor fitting and extrapolation to $Q^2 = 0$. Some recent calculations for the proton isovector electromagnetic radii are shown in Fig. 6, and the proton charge radius results are shown in Fig. 7. Despite many difficulties such as finite lattice size and contamination from excited states, the lattice QCD community continues to make important progress and the precision starts to approach that from the electron scattering experiments. Yet, higher precision lattice calculations are still needed in order to fully understand the proton charge radius puzzle. Other than the radius, low Q^2 proton electric form factor can be very interesting by itself, given the large discrepancy observed between the PRad data [3] and the Mainz 2010 data [2], particularly in the Q^2 region between 0.01 GeV² to 0.06 GeV² (see Fig 4). Even though lattice calculation in the very low Q^2 region is very difficult, as one would need a very large lattice

setup, high precision lattice calculations in this low Q^2 range are very interesting and can be an important input to this data tension in the lepton-scattering community. More information about recent progress for nucleon form factors and radii can be found in the proceeding by Djukanovic [68].

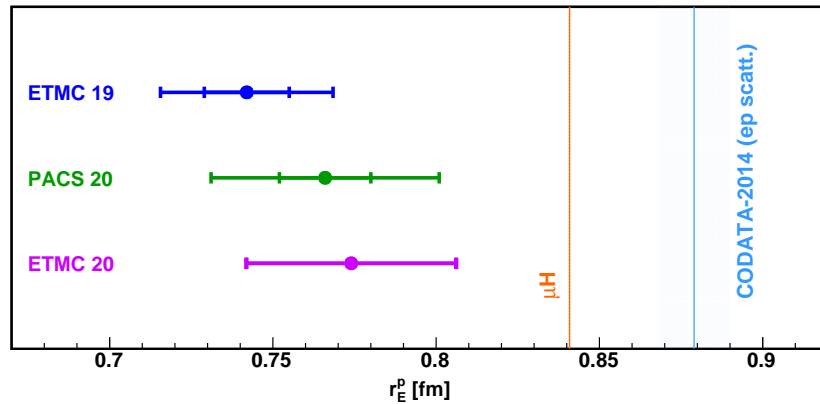


Figure 7. The proton charge radius r_E^p from recent lattice QCD calculations [38,40,41], and compared to the μ H measurement [11] and the CODATA-2014 recommended value [69]. ETMC 19 calculation [38] includes disconnected contributions.

5. Remaining Issues in Lepton Scattering Experiments and Possible Explanation

Although numerous re-analyses and world data fitting studies have been performed since 2010, and Lattice QCD have been making major improvements during the meantime, the proton charge radius puzzle is still considered unresolved by many physicists, especially from the scattering community. First of all, PRad experiment [3] is the only new unpolarized lepton scattering experiment, with a precision high enough to impact the puzzle, since 2010. Its result is consistent with the μ H measurement, but the conflict between PRad and other modern scattering experiments calls for at least one other experiment, with different kinematics and systematics to cross-check. In addition to the r_E^p puzzle, the observed G_E^p data tension between the Mainz 2010 and PRad experiments needs to be investigated and understood. This discrepancy exists in the lower Q^2 region already, but it is more prominent at the higher Q^2 from 0.01 GeV² to 0.06 GeV².

A number of possible factors might explain this data tension. First of all, some recent re-analyses [62,63] show that using a more constrained functional form to fit the cross-section data could lead to a different set of normalization parameters and G_E^p , which makes the discrepancy much smaller. The radiative correction could also possibly contribute to the discrepancy, for which both PRad and Mainz 2010 experiments relied on full simulations of the radiative effects but followed different recipes of the internal radiative correction. PRad used the complete first-order calculations beyond URA from Akushevich [54], while Mainz followed the recipes from Maximon-Tjon [71] and Vanderhaeghen [72]. Both experiments achieved a sub-percent agreement between the simulation and data [60,73], but the PRad experiment found out that the neglected next-to-next leading order (NNLO) contributions, especially for the Møller process, would contribute significantly to the total systematic uncertainty of the radius extraction because of large leverage due to the kinematic dependence. This finding motivated improved calculations of QED radiative effects for the future PRad-II experiment. Third, the proton magnetic form factor and r_M^p may affect the electric form factor and the charge radius. As shown in Eq. 3, the ep elastic cross-section contains contributions from both G_E^p and G_M^p . Assuming the cross-section measurements are accurate, then a smaller G_E^p will certainly

lead to a larger G_M^p at the same kinematics. There is indeed a less well-known discrepancy in this area. As pointed out by Lee *et al.* [30], there is a 2.7σ difference between r_M^p extracted from world data excluding the Mainz 2010 results, and the Mainz 2010 data alone. Lastly, overlooked or underestimated systematic uncertainties associated with different experimental apparatus between these experiments could also be a possibility. For instance, the high Q^2 region of the PRad data was covered by lead glass detectors, which were less reliable compared to the inner PbWO_4 modules of the calorimeter, and hence more conservative systematic uncertainties had to be assigned for data points in this region. Fortunately, many future experiments, which we will discuss in the following section, plan to use different and advanced target and detector systems to have better control over these types of systematics.

6. Future Lepton-proton Scattering Experiments

Motivated by the unresolved proton charge radius puzzle and the form factor data tension, many new lepton-proton elastic scattering experiments are currently under preparation or taking data. Most of these new experiments will cover the low Q^2 region, where the PRad data and the Mainz 2010 data show a large discrepancy (see Fig. 8). These new experiments use vastly different experimental techniques and all have very unique features. They will be able to provide different inputs to address the remaining issues in the field. In the following subsections, we will introduce the experimental design and special features of these next-generation experiments that focus on low- Q^2 lepton-proton elastic scattering. Similar details can also be found in recent reviews by Gao and Vanderhaeghen [1], and also Karr, Marchand, and Voutier [74].

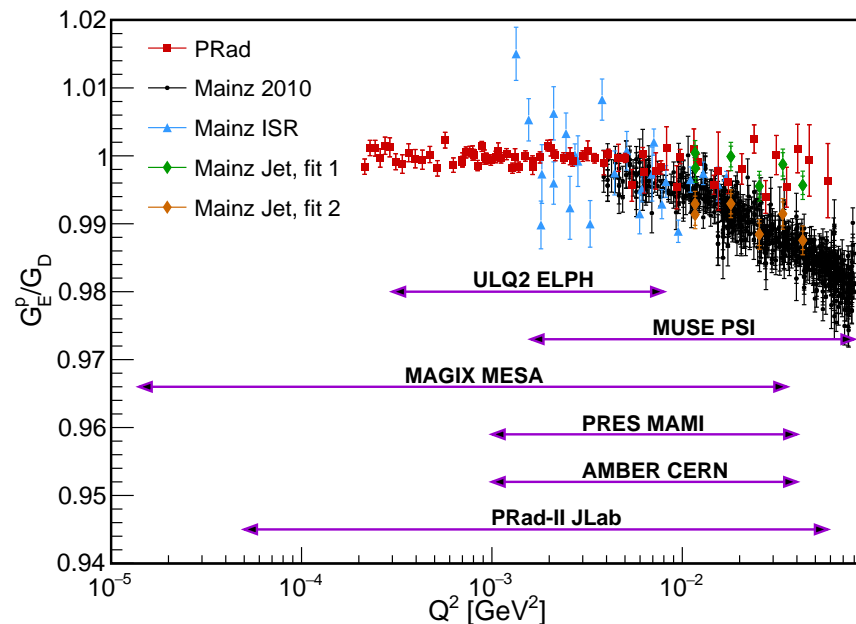


Figure 8. The proton electric form factor, normalized by the standard dipole form factor, from the PRad experiment [3] (red squared), the Mainz 2010 experiment [2] (black dots), the Mainz ISR experiment [4] (blue triangles), and Mainz jet target experiment [45], where green diamonds are fitted to PRad parameterization and orange diamonds are fitted to Mainz 2010 parameterization. Also shown on top, are the expected Q^2 coverages from future experiments including MUSE [75,76], PRad-II [77], AMBER [78,79], PRES [80,81], MAGIX [55] and ULQ2 experiments [82,83].

6.1. MUSE Experiment

So far, all proton charge radius results measured using the scattering technique are obtained with electrons as the incident leptons. The first r_E^p measurement using the muon is expected to come from the MUon Scattering Experiment (MUSE) [75,76], which is currently taking data at Paul Scherrer Institut (PSI). This experiment aims to measure the lepton-proton elastic scattering cross-sections using e^- , μ^- , as well as e^+ and μ^+ , and data with the same beam polarity, can be collected simultaneously. This unique experiment will be able to provide a couple of valuable insights into the proton charge radius puzzle. On one hand, a comparison between the electronic and muonic measurements will be a direct test for the lepton-universality violation and all related new physics. On the other hand, this comparison can also test our understanding of radiative corrections (RC). Given nearly 200 times larger mass relative to electrons, muons have much smaller radiative effects. If there is a systematic difference between the electronic and the muonic measurements, this could indicate certain issues with RC, which is one of the main suspects for the discrepancy between the PRad data and earlier measurements. In addition, the usage of both positive and negative polarities of the incoming lepton beam allows one to control the contribution from the two-photon-exchange (TPE) diagrams [84,85], which might contribute to the cross-section no more than 1% [76], depending on the kinematics. This contribution is notoriously difficult to precisely calculate but can be effectively constrained by taking the difference between cross-sections with different beam polarities.

The MUSE experiment uses the π M1 beamline at PSI, and the lepton-proton elastic scattering cross-sections are measured with three different beam energies, at 115, 161, and 210 MeV. This beamline provides a mixture of pions, muons, and electrons, so it is critical for the experiment to have an excellent particle identification (PID) for the incident particles, especially given that the pions will be the dominant species. In addition, many properties of the beam, such as emittance and momentum bite, are also not as good as that of modern primary electron beams [86]. To overcome these difficulties, the experiment is equipped with a beam hodoscope (shown in Fig. 9) for precise timing measurements as the incident particles pass through. The time-of-flight obtained by combining these measurements with information from the accelerator RF can provide a precise PID. Three GEM detectors are placed immediately after the hodoscope to determine precisely the incident angles. These are high-resolution tracking devices with high rate capacities, and can easily achieve an angular resolution at the level of 1 mrad. In between the GEMs and the target chamber, a veto scintillator detector is used to reduce background and reject particles that have decayed in flight. The target chamber contains three different targets: a liquid hydrogen target used for physics production, an empty target for background studies, as well as a carbon target for detector alignments. After the un-scattered beam exits the chamber, it will reach the downstream beam monitor that provides measurements for the flux and additional timing information, and then eventually the calorimeter, which can be used to control radiative effects, particularly those from the initial state radiation (shown in left panel of Fig. 2). On the other hand, the scattered lepton will exit the target chamber through the side walls, with their scattering angles measured by the straw-tube trackers, and timing measured by the scattered particle scintillators.

This detector setup provides a scattering-angle coverage from 20° to 100° , an azimuthal-angle coverage of about 30% of 2π . With the three beam energies mentioned above, the experimental apparatus covers a Q^2 range from 0.0016 to about 0.08 GeV^2 . The expected statistical uncertainty is better than 1% for the cross-section measurements, and the uncertainty on r_E^p is expected to be at the level of 0.01 fm, for all four different incident particle species. The MUSE experiment is currently taking data, and the results are highly anticipated due to its various unique features.

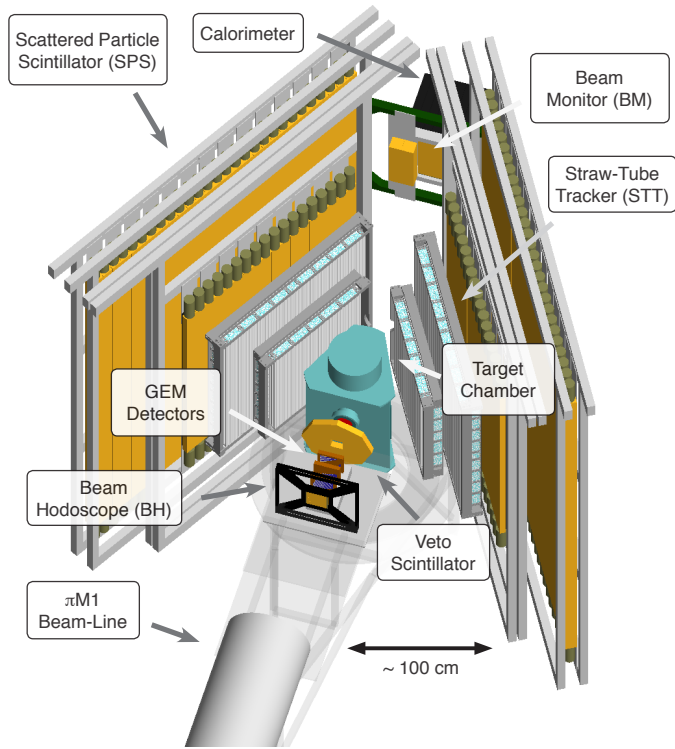


Figure 9. The experimental apparatus of the MUSE experiment. Figure credit: Steffen Strauch.

6.2. PRad-II Experiment

The PRad-II experiment at Jefferson Lab [77] has been fully approved by the Jefferson Lab program advisory committee (PAC), and received the highest scientific rate “A”. This new-generation experiment will inherit all the advantages of the original PRad experiment, including the non-magnetic calorimetric configuration and the windowless target. More importantly, it aims to reduce the total uncertainties of r_E^p and G_E^p by about a factor of 4, with major improvements on the experimental apparatus and analysis method. This will not only reach an unprecedented precision of r_E^p (0.0036 fm) from scattering experiments but also, more importantly, will help to address the tension between the PRad G_E^p data with the previous Mainz 2010 measurements.

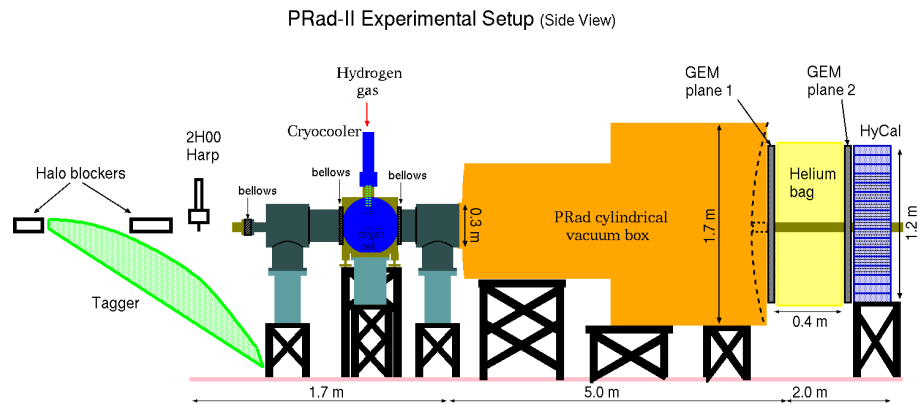


Figure 10. The experimental apparatus of the PRad-II experiment. Figure credit: A. Gasparian *et al.* [77]

The experimental apparatus of PRad-II is shown in Fig. 10. The first major improvement comes from the addition of a second GEM plane. When separated by 40 cm from the other GEM plane, they provide a large enough leverage and a reasonable vertex- z reconstruction in order to reject the majority of beamline backgrounds coming from upstream of the target. Another advantage of having a second GEM plane is that the GEM efficiencies can be measured much more precisely as information about the incident angles will be provided by another GEM plane, instead of the HyCal. In the case of PRad, the HyCal position resolution (at the level of a few millimeters at best) was a limiting factor for the GEM efficiency measurement. As a result, in the forward angular range, the cross-section measurements had to rely completely on the cancellation from taking the ep/ee yield ratio (the bin-by-bin method) in the same angular bin. While this method is rather effective in canceling the energy-independent part of the detector acceptance and efficiency, it may introduce Q^2 -dependent systematic uncertainties from Møller scatterings into the ep cross-section. Having more precise knowledge about GEM efficiencies will allow another method, the integrated Møller method, to be applied for the entire ep kinematic range. In this method, a fixed angular range will be selected, and all the Møller yields within the range will be used as a common normalization factor for all ep angular bins. In the integrated Møller method, there is no cancellation for the efficiencies, and Møller yield is only used to cancel out the luminosity. However, the advantage is that all systematic uncertainties from Møller now only affect the normalization, and will not impact r_E^p . The second major improvement comes from replacing all lead-glass modules with lead-tungsten modules. The lead-glass modules covered the large angular range or the high- Q^2 region of the PRad experiment. These modules have about 2.5 times worse energy resolution compared to the lead-tungsten modules and have shown to be insufficient in rejecting the inelastic ep scattering backgrounds. Furthermore, they also have much larger non-linearity responses for energy depositions of the scattered electrons. These led to some of the most dominating systematic uncertainties for the cross-section results in the high Q^2 region of the PRad data. Given the large discrepancy between the PRad results and the Mainz 2010 results in this particular Q^2 region. It is thus, critical to replace all the lead-glass modules, and use a fully uniform lead-tungsten calorimeter for the PRad-II experiment. Thirdly, the PRad-II setup includes a new scintillating detector, placed inside the target chamber and 25 cm downstream from the target center. The purpose of this detector is to separate Møller and ep events in the very forward angular range, particularly for the lowest energy setting. Given that the energy of scattered electrons from these two processes starts to converge as the scattering angle decreases, the calorimeter can no longer effectively separate them below 0.7° for the 1.101 GeV data set of PRad, even with the excellent energy resolution of the lead-tungsten modules. In principle, one may still be able to identify Møller events if both electrons in the final state are detected. But in this particular kinematic range, the lower energy electron from the Møller process tends to fly out of the acceptance of HyCal. This is precisely the purpose of having the new scintillating detector, which will be able to detect those low-energy Møller electrons and separate these Møller events from ep elastic scattering events. This will help the setup to extend its lowest angular coverage down to about 0.5° or $\sim 5 \times 10^{-5} \text{ GeV}^2$, breaking the lowest Q^2 record set by the original PRad experiment ($2.1 \times 10^{-4} \text{ GeV}^2$).

Other than detector upgrades, the collaboration also plans to replace the Fastbus readout system of the calorimeter with a full flash-ADC-based readout, which will allow a much larger event-rate capacity. In addition, this new system can also measure the pedestal noise event-by-event, and provide a much better timing measurement to reject accidentals and improve the trigger efficiency. In addition, the collaboration also seeks to improve the RC calculation by including NNLO diagrams for both the ep and Møller scatterings, beyond the ultra-relativistic approximation where the electron mass is not neglected [87]. This is expected to significantly reduce the r_E^p systematic uncertainty from RC. If using the integrated Møller method, the total

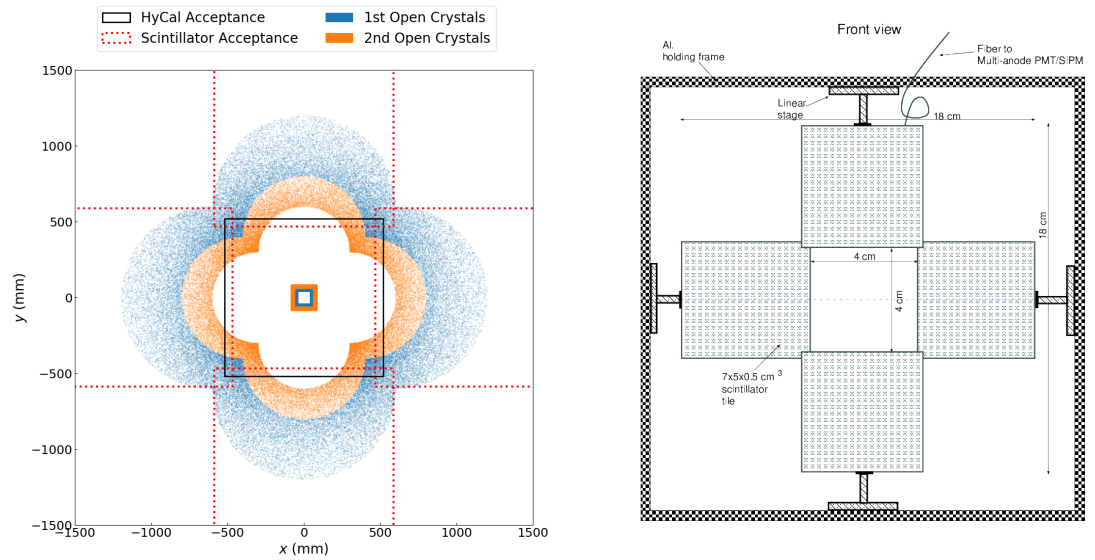


Figure 11. Left panel: The distribution of Møller electrons, when the other one is detected by the two opened innermost layers of HyCal. Red dash lines show the boundaries of the scintillator tiles. **Right panel:** A schematic view of the scintillator detector to enhance detection of the Møller electrons. Figure credit: A. Gasparian *et al.* [77]

systematic uncertainty from RC is expected to be negligible, compared to the total uncertainty of r_E^p .

The PRad-II experiment plans to take data using 0.7, 1.4 and 2.1 GeV electron beams, which covers Q^2 from $\sim 5 \times 10^{-5} \text{ GeV}^2$ to 0.056 GeV^2 . With about 24 days of production runs, the expected statistical uncertainties on the r_E^p will be about 0.0017 fm, which is about 4.4 times smaller than that of PRad. The collaboration has also done a comprehensive analysis for the projected systematic uncertainty, considering all aspects based on experience from the PRad experiment. When summed in quadrature, the total uncertainty on r_E^p is about 0.0036 fm, which is nearly 4 times smaller than that of PRad.

6.3. Compass++/AMBER Experiment

Another experiment that will use a muon beam is the AMBER experiment [78,79], which has already been approved by CERN and will be built based on the legacy of COMPASS. This experiment will use mainly a 100 GeV muon beam, produced by the M2 beam line of the Super Proton Synchrotron (SPS) at CERN. The very low Q^2 range ($0.001 \text{ GeV}^2 < Q^2 < 0.04 \text{ GeV}^2$) can be reached by measuring the scattered muons in the extreme forward angular region (at the level of 1 mrad). These particular features will minimize the magnetic factor G_M^p contribution to the cross-section, as well as smaller radiative effects. However, the resolution for the scattering angle becomes critical and needs to be controlled below $100 \mu\text{rad}$ in order to measure Q^2 down to 0.001 GeV^2 . To ensure this, the experimental setup includes two telescope arms to measure the incident and scattered muons. Each telescoping arm has two silicon detectors around the entrance and exit, and the length is about 5 m long to provide sufficient leverage for the angle reconstruction. Most of the space in between the silicon detectors will be occupied by a helium or vacuum tube to further reduce the material and multiple scatterings. The central region of the setup is a Time Projection Chamber (TPC), which will be filled with pressurized hydrogen gas up to 20 bar. The TPC will serve as an active target, and also measure the recoiled proton with energy varied from 0.5 MeV to 20 MeV. The trigger of the setup will be produced by the

muons when they pass through the fiber triggers. With about 260 days of measurement, the projected statistical uncertainty will be better than 0.1% for the proton electric form factor G_E^p , and better than 0.01 fm for the precision of the proton charge radius [79].

6.4. The PRES Experiment at Mainz

The Mainz PRES experiment [80,81] will use a very similar experimental setup to the AMBER experiment. The PRES experiment will be performed in the A2 experimental hall of Mainz Microtron, using a 720 MeV high-precision electron beam. Similar to the AMBER experiment, a TPC filled with pressurized, high-purity, hydrogen gas will be used as an active target [88]. It will also be able to detect the recoil protons, which provides a number of advantages. First, Q^2 in ep elastic scattering can be reconstructed using the proton energy alone, independent of the energy of incident electrons. In this way, the reconstructed Q^2 is not sensitive to any pre-vertex energy loss of the electron beam (such as energy loss when the electron beam goes through the TPC entrance window), as well as the uncertainty in the electron beam energy. Secondly, having Q^2 reconstructed by proton will largely suppress certain radiative effects such as real-photon bremsstrahlung from the electron line and the electron vertex correction. These are some of the dominating radiative effects for traditional ep scattering experiments, in which only the scattered electrons are measured. In addition, the scattered electrons will also be detected in coincidence by a MWPC-based forward tracker. With 45 days of data taking, about 70 million $e-p$ elastic events will be collected, covering a Q^2 range between 0.001 GeV² and 0.04 GeV². The differential cross-sections are expected to have 0.1% relative and 0.2% absolute precisions [80], and the expected total uncertainty on r_E^p will be better than 0.01 fm.

6.5. Mainz MAGIX Experiment

Another future experiment at Mainz is the MAInz Gas Injection target eXperiment (MAGIX) [55]. This experiment will use the Mainz Superconducting Energy Recovery Linac (MESA) [89], which is currently under construction. For the MAGIX experiment, the accelerator plans to run in its Energy Recovery Linac (ERL) mode, which can provide a 1 mA electron beam current with energy up to 105 MeV. The experiment will use an internal cryogenic supersonic gas jet target [55]. A target of this type has already been developed and used successfully in the Mainz jet target experiment [45] (discussed in Ch. 3.3). This powerful new technique brings various benefits, such as minimizing pre-vertex radiative effects and multiple scattering, eliminating backgrounds generated from traditional target cell windows, and being effectively a point-like target. The integrated luminosity will be in the order of 10³⁵ cm⁻²s⁻¹ [55].

The MAGIX experiment will employ a multi-purpose spectrometer system as shown in Fig. 12¹. The target chamber is at the center and is connected to a pair of identical magnetic spectrometers with a movable vacuum seal in order to reduce material effects [90]. Each spectrometer arm has a wide angular coverage (15° to 165°) with respect to the beamline and contains a quadrupole magnet, followed by two dipole magnets, which will bend and focus the final-state particles into the focal plane detectors. This detector array contains a GEM-based TPC for tracking and high-rate capacity, as well as a trigger veto system that is made of a plastic scintillation detector and a flexible system of additional scintillation detectors and lead absorbers. To further reduce the material effects, the focal plane detectors adopt an open field-cage design for the TPC [90], with an open face pointing towards the spectrometer vacuum chamber. This spectrometer system will be able to achieve a relative momentum resolution $\sim 10^{-4}$, and an angular resolution of about 1 mrad.

¹ This figure is contained in the article that was published by B. S. Schlimme *et al.* [A1 and MAGIX], "Operation and characterization of a windowless gas jet target in high-intensity electron beams," Nucl. Instrum. Meth. A **1013**, 165668 (2021), Copyright Elsevier 2023.

With the low beam energy of the MESA accelerator, the MAGIX experiment will be able to achieve the lowest Q^2 of about 10^{-4} GeV^2 , and the highest Q^2 about 0.03 GeV^2 . The relative precision on the proton electric form factor will be mostly below 0.1% . At the same time, the experiment also has a strong sensitivity on the magnetic form factor, aiming to achieve an order of magnitude better precision in the low Q^2 region [91].

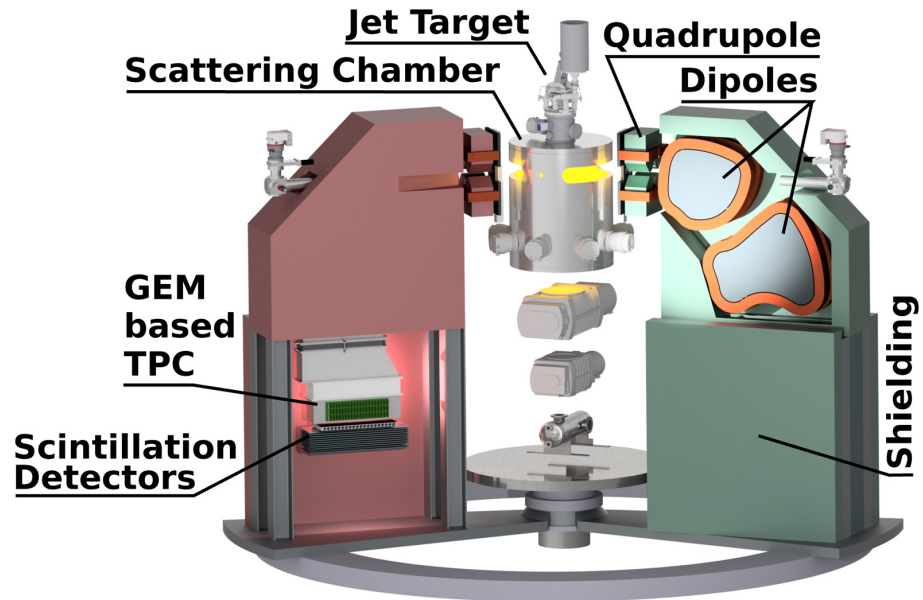


Figure 12. The multi-purpose spectrometer system planned for the MAGIX experiment (figure credit: B. S. Schlimme *et al.* [55]).

6.6. ULQ2 Experiment

The Ultra-Low Q^2 (ULQ2) collaboration [82,83] plans to carry out an electron scattering experiment at the Research Center for ELectron PHoton Science (ELPH) of Tohoku University, Japan. Using a low-energy electron linac, an electron beam of energy between 20 MeV to 60 MeV will be used to measure the ep elastic scattering cross-section, covering Q^2 from 3×10^{-4} GeV^2 to 8×10^{-3} GeV^2 . The scattered electrons will be measured by magnetic spectrometers with Single-Sided Silicon Detectors (SSSD) as the focal plane detectors. These spectrometers have a relative momentum resolution of $\sim 10^{-3}$ and a scattering angle coverage from 30° to 150° . A CH_2 target will be used for this experiment, and the well-established elastic $e-^{12}\text{C}$ cross-section will be measured simultaneously in order to normalize the ep elastic scattering cross-section. This experiment will also have a strong sensitivity on the proton magnetic form factor, and the Rosenbluth separation will be performed to extract G_E^p and G_M^p from the cross-section measurements. The expected uncertainty on the extracted G_E^p is at the level of 10^{-3} .

7. Conclusion and Outlook

In this paper, we reviewed recent progress on the proton charge radius puzzle and low- Q^2 proton electric form factor measurements from ep elastic scattering experiments. Although the recent high precision r_E^p measurement from the PRad experiment [3] is consistent with the μH spectroscopic results [10,11], it is only 3σ away from the CODATA-2010 recommended value [18]. More importantly, the lepton scattering community certainly needs to understand the form factor G_E^p difference between the PRad data and the previous scattering data within $0.01 < Q^2 < 0.06$ GeV^2 . Many new lepton-proton elastic scattering experiments, motivated by the radius puzzle, have been taking data or are under preparation. They all have very unique

features and systematics, and hence will be able to shed light on the puzzle and the observed data tension on the proton electric form factor. In the meantime, the recent development on the theoretical side, including the modern extraction methods for proton charge radius and *ab-initio* calculations from Lattice QCD, is promising and exciting. With these dedicated efforts, our knowledge about the proton charge radius will be deepened in the next decade. By that time, hopefully, all the above-mentioned puzzles will be resolved in a satisfactory way.

Author Contributions: Both authors contribute equally to the draft preparation, review and editing. Both authors have read and agreed to the published version of the manuscript.

Funding: The work of Chao Peng is supported in part by the U.S. Department of Energy, Office of Science, Office of Nuclear Physics, under Contract No. DE-AC02-06CH11357.

Institutional Review Board Statement: Not applicable.

Data Availability Statement: Not applicable.

Acknowledgments: The authors would like to thank Haiyan Gao, Ashot Gasparian, Dipangkar Dutta, Jingyi Zhou, Jan Bernauer and Björn Sören Schlimme, for helpful discussion, and Steffen Strauch for making the figure for the MUSE experiment.

Conflicts of Interest: The authors declare no conflict of interest.

References

1. H. Gao and M. Vanderhaeghen, *Rev. Mod. Phys.* **94**, no.1, 015002 (2022) doi:10.1103/RevModPhys.94.015002 [arXiv:2105.00571 [hep-ph]].
2. J. C. Bernauer *et al.* [A1], *Phys. Rev. Lett.* **105**, 242001 (2010) doi:10.1103/PhysRevLett.105.242001 [arXiv:1007.5076 [nucl-ex]].
3. W. Xiong, A. Gasparian, H. Gao, D. Dutta, M. Khandaker, N. Liyanage, E. Pasyuk, C. Peng, X. Bai and L. Ye, *et al.* *Nature* **575**, no.7781, 147-150 (2019) doi:10.1038/s41586-019-1721-2
4. M. Mihovilovič, P. Achenbach, T. Beranek, J. Beričič, J. C. Bernauer, R. Böhm, D. Bosnar, M. Cardinali, L. Correa and L. Debenjak, *et al.* *Eur. Phys. J. A* **57**, no.3, 107 (2021) doi:10.1140/epja/s10050-021-00414-x [arXiv:1905.11182 [nucl-ex]].
5. X. Zhan, K. Allada, D. S. Armstrong, J. Arrington, W. Bertozzi, W. Boeglin, J. P. Chen, K. Chirapatpimol, S. Choi and E. Chudakov, *et al.* *Phys. Lett. B* **705**, 59-64 (2011) doi:10.1016/j.physletb.2011.10.002 [arXiv:1102.0318 [nucl-ex]].
6. A. J. R. Puckett, E. J. Brash, M. K. Jones, W. Luo, M. Mezziane, L. Pentchev, C. F. Perdrisat, V. Punjabi, F. R. Wesselmann and A. Ahmidouch, *et al.* *Phys. Rev. Lett.* **104**, 242301 (2010) doi:10.1103/PhysRevLett.104.242301 [arXiv:1005.3419 [nucl-ex]].
7. C. B. Crawford, A. Sindile, T. Akdogan, R. Alarcon, W. Bertozzi, E. Booth, T. Botto, J. Calarco, B. Clasić and A. DeGrush, *et al.* *Phys. Rev. Lett.* **98**, 052301 (2007) doi:10.1103/PhysRevLett.98.052301 [arXiv:nucl-ex/0609007 [nucl-ex]].
8. Y. H. Lin, H. W. Hammer and U. G. Meißner, *Phys. Rev. Lett.* **128**, no.5, 052002 (2022) doi:10.1103/PhysRevLett.128.052002 [arXiv:2109.12961 [hep-ph]].
9. M. Ablikim *et al.* [BESIII], *Phys. Lett. B* **817**, 136328 (2021) doi:10.1016/j.physletb.2021.136328 [arXiv:2102.10337 [hep-ex]].
10. R. Pohl, A. Antognini, F. Nez, F. D. Amaro, F. Biraben, J. M. R. Cardoso, D. S. Covita, A. Dax, S. Dhawan and L. M. P. Fernandes, *et al.* *Nature* **466**, 213-216 (2010) doi:10.1038/nature09250
11. A. Antognini, F. Nez, K. Schuhmann, F. D. Amaro, Francois Biraben, J. M. R. Cardoso, D. S. Covita, A. Dax, S. Dhawan and M. Diepold, *et al.* *Science* **339**, 417-420 (2013) doi:10.1126/science.1230016
12. A. Beyer, L. Maisenbacher, A. Matveev, R. Pohl, K. Khabarova, A. Grinin, T. Lamour, D. C. Yost, T. W. Hänsch and N. Kolachevsky, *et al.* *Science* **358**, no.6359, 79-85 (2017) doi:10.1126/science.aah6677
13. H. Fleurbaey, S. Galtier, S. Thomas, M. Bonnaud, L. Julien, F. Biraben, F. Nez, M. Abgrall and J. Guéna, *Phys. Rev. Lett.* **120**, no.18, 183001 (2018) doi:10.1103/PhysRevLett.120.183001 [arXiv:1801.08816 [physics.atom-ph]].
14. N. Bezginov, T. Valdez, M. Horbatsch, A. Marsman, A. C. Vutha and E. A. Hessels, *Science* **365**, no.6457, 1007-1012 (2019) doi:10.1126/science.aau7807
15. A. Grinin, A. Matveev, D. C. Yost, L. Maisenbacher, V. Wirthl, R. Pohl, T. W. Hänsch and T. Udem, *Science* **370** no.6520 1061-1066 (2020) doi:10.1126/science.abc7776
16. A. D. Brandt, S. F. Cooper, C. Rasoar, Z. Burkley, D. C. Yost and A. Matveev, *Phys. Rev. Lett.* **128**, no.2, 023001 (2022) doi:10.1103/PhysRevLett.128.023001 [arXiv:2111.08554 [physics.atom-ph]].
17. G. A. Miller, *Phys. Rev. C* **99**, no.3, 035202 (2019) doi:10.1103/PhysRevC.99.035202 [arXiv:1812.02714 [nucl-th]].

18. P. J. Mohr, B. N. Taylor and D. B. Newell, *Rev. Mod. Phys.* **84**, 1527-1605 (2012) doi:10.1103/RevModPhys.84.1527 [arXiv:1203.5425 [physics.atom-ph]].
19. C. E. Carlson and M. Vanderhaeghen, *Phys. Rev. A* **84**, 020102 (2011) doi:10.1103/PhysRevA.84.020102 [arXiv:1101.5965 [hep-ph]].
20. M. Gorchtein, F. J. Llanes-Estrada and A. P. Szczepaniak, *Phys. Rev. A* **87**, no.5, 052501 (2013) doi:10.1103/PhysRevA.87.052501 [arXiv:1302.2807 [nucl-th]].
21. O. Tomalak, *Eur. Phys. J. A* **55**, no.5, 64 (2019) doi:10.1140/epja/i2019-12743-1 [arXiv:1808.09204 [hep-ph]].
22. M. C. Birse and J. A. McGovern, *Eur. Phys. J. A* **48**, 120 (2012) doi:10.1140/epja/i2012-12120-8 [arXiv:1206.3030 [hep-ph]].
23. C. Peset and A. Pineda, *Eur. Phys. J. A* **51**, no.12, 156 (2015) doi:10.1140/epja/i2015-15156-2 [arXiv:1508.01948 [hep-ph]].
24. R. J. Hill and G. Paz, *Phys. Rev. D* **95**, no.9, 094017 (2017) doi:10.1103/PhysRevD.95.094017 [arXiv:1611.09917 [hep-ph]].
25. Y. Fu, X. Feng, L. C. Jin and C. F. Lu, *Phys. Rev. Lett.* **128**, no.17, 172002 (2022) doi:10.1103/PhysRevLett.128.172002 [arXiv:2202.01472 [hep-lat]].
26. C. E. Carlson, *Prog. Part. Nucl. Phys.* **82**, 59-77 (2015) doi:10.1016/j.pnnp.2015.01.002 [arXiv:1502.05314 [hep-ph]].
27. Y. S. Liu and G. A. Miller, *Phys. Rev. D* **96**, no.1, 016004 (2017) doi:10.1103/PhysRevD.96.016004 [arXiv:1705.01633 [hep-ph]].
28. Y. S. Liu, I. C. Cloët and G. A. Miller, *Nucl. Phys. B*, 114638 (2019) doi:10.1016/j.nuclphysb.2019.114638 [arXiv:1805.01028 [hep-ph]].
29. J. Bordes, H. M. Chan and S. T. Tsou, *Int. J. Mod. Phys. A* **34**, no.25, 1950140 (2019) doi:10.1142/S0217751X19501409 [arXiv:1906.09229 [hep-ph]].
30. G. Lee, J. R. Arrington and R. J. Hill, *Phys. Rev. D* **92**, no.1, 013013 (2015) doi:10.1103/PhysRevD.92.013013 [arXiv:1505.01489 [hep-ph]].
31. D. W. Higinbotham, A. A. Kabir, V. Lin, D. Meekins, B. Norum and B. Sawatzky, *Phys. Rev. C* **93**, no.5, 055207 (2016) doi:10.1103/PhysRevC.93.055207 [arXiv:1510.01293 [nucl-ex]].
32. K. Griffioen, C. Carlson and S. Maddox, *Phys. Rev. C* **93**, no.6, 065207 (2016) doi:10.1103/PhysRevC.93.065207 [arXiv:1509.06676 [nucl-ex]].
33. X. Yan, D. W. Higinbotham, D. Dutta, H. Gao, A. Gasparian, M. A. Khandaker, N. Liyanage, E. Pasyuk, C. Peng and W. Xiong, *Phys. Rev. C* **98**, no.2, 025204 (2018) doi:10.1103/PhysRevC.98.025204 [arXiv:1803.01629 [nucl-ex]].
34. E. Kraus, K. E. Mesick, A. White, R. Gilman and S. Strauch, *Phys. Rev. C* **90**, no.4, 045206 (2014) doi:10.1103/PhysRevC.90.045206 [arXiv:1405.4735 [nucl-ex]].
35. J. M. Alarcón, D. W. Higinbotham and C. Weiss, *Phys. Rev. C* **102**, no.3, 035203 (2020) doi:10.1103/PhysRevC.102.035203 [arXiv:2002.05167 [hep-ph]].
36. Z. F. Cui, D. Binosi, C. D. Roberts and S. M. Schmidt, *Phys. Rev. Lett.* **127**, no.9, 092001 (2021) doi:10.1103/PhysRevLett.127.092001 [arXiv:2102.01180 [hep-ph]].
37. N. Hasan, J. Green, S. Meinel, M. Engelhardt, S. Krieg, J. Negele, A. Pochinsky and S. Syritsyn, *Phys. Rev. D* **97**, no.3, 034504 (2018) doi:10.1103/PhysRevD.97.034504 [arXiv:1711.11385 [hep-lat]].
38. C. Alexandrou, S. Bacchio, M. Constantinou, J. Finkenrath, K. Hadjiyiannakou, K. Jansen, G. Koutsou and A. Vaquero Aviles-Casco, *Phys. Rev. D* **100**, no.1, 014509 (2019) doi:10.1103/PhysRevD.100.014509 [arXiv:1812.10311 [hep-lat]].
39. Y. C. Jang, R. Gupta, H. W. Lin, B. Yoon and T. Bhattacharya, *Phys. Rev. D* **101**, no.1, 014507 (2020) doi:10.1103/PhysRevD.101.014507 [arXiv:1906.07217 [hep-lat]].
40. E. Shintani, K. I. Ishikawa, Y. Kuramashi, S. Sasaki and T. Yamazaki, *Phys. Rev. D* **99**, no.1, 014510 (2019) [erratum: *Phys. Rev. D* **102**, no.1, 019902 (2020)] doi:10.1103/PhysRevD.99.014510 [arXiv:1811.07292 [hep-lat]].
41. C. Alexandrou, K. Hadjiyiannakou, G. Koutsou, K. Ottnad and M. Petschlies, *Phys. Rev. D* **101**, no.11, 114504 (2020) doi:10.1103/PhysRevD.101.114504 [arXiv:2002.06984 [hep-lat]].
42. K. I. Ishikawa *et al.* [PACS], *Phys. Rev. D* **104**, no.7, 074514 (2021) doi:10.1103/PhysRevD.104.074514 [arXiv:2107.07085 [hep-lat]].
43. S. Park *et al.* [Nucleon Matrix Elements (NME)], *Phys. Rev. D* **105**, no.5, 054505 (2022) doi:10.1103/PhysRevD.105.054505 [arXiv:2103.05599 [hep-lat]].
44. D. Djukanovic, T. Harris, G. von Hippel, P. M. Junnarkar, H. B. Meyer, D. Mohler, K. Ottnad, T. Schulz, J. Wilhelm and H. Wittig, *Phys. Rev. D* **103**, no.9, 094522 (2021) doi:10.1103/PhysRevD.103.094522 [arXiv:2102.07460 [hep-lat]].
45. Y. Wang *et al.* [A1 and MAGIX], *Phys. Rev. C* **106**, no.4, 044610 (2022) doi:10.1103/PhysRevC.106.044610 [arXiv:2208.13689 [nucl-ex]].
46. E. Tiesinga, P. J. Mohr, D. B. Newell and B. N. Taylor, *Rev. Mod. Phys.* **93**, no.2, 025010 (2021) doi:10.1103/RevModPhys.93.025010
47. A. V. Gramolin, V. S. Fadin, A. L. Feldman, R. E. Gerasimov, D. M. Nikolenko, I. A. Rachek and D. K. Toporkov, *J. Phys. G* **41**, no.11, 115001 (2014) doi:10.1088/0954-3899/41/11/115001 [arXiv:1401.2959 [nucl-ex]].
48. H. Atac, M. Constantinou, Z. E. Mezziani, M. Paolone and N. Sparveris, *Eur. Phys. J. A* **57**, no.2, 65 (2021) doi:10.1140/epja/s10050-021-00389-9 [arXiv:2009.04357 [nucl-ex]].
49. A. V. Gramolin and R. L. Russell, *Phys. Rev. D* **105**, no.5, 054004 (2022) doi:10.1103/PhysRevD.105.054004 [arXiv:2102.13022 [nucl-ex]].
50. L. W. Mo and Y. S. Tsai, *Rev. Mod. Phys.* **41**, 205-235 (1969) doi:10.1103/RevModPhys.41.205
51. J. Pierce, J. Brock, C. Carlin, C. Keith, J. Maxwell, D. Meekins, X. Bai, A. Deur, D. Dutta and H. Gao, *et al.* *Nucl. Instrum. Meth. A* **1003**, 165300 (2021) doi:10.1016/j.nima.2021.165300 [arXiv:2103.01749 [physics.ins-det]].
52. X. Bai, doi:10.18130/v3-k8q4-z887

53. S. Agostinelli *et al.* [GEANT4], Nucl. Instrum. Meth. A **506**, 250-303 (2003) doi:10.1016/S0168-9002(03)01368-8
54. I. Akushevich, H. Gao, A. Ilyichev and M. Mezziane, Eur. Phys. J. A **51**, no.1, 1 (2015) doi:10.1140/epja/i2015-15001-8
55. B. S. Schlimme *et al.* [A1 and MAGIX], Nucl. Instrum. Meth. A **1013**, 165668 (2021) doi:10.1016/j.nima.2021.165668 [arXiv:2104.13503 [physics.ins-det]].
56. A. Schmidt, [arXiv:1711.09894 [nucl-ex]].
57. J. J. Kelly, Phys. Rev. C **70**, 068202 (2004) doi:10.1103/PhysRevC.70.068202
58. T. B. Hayward and K. A. Griffioen, Nucl. Phys. A **999**, 121767 (2020) doi:10.1016/j.nuclphysa.2020.121767 [arXiv:1804.09150 [nucl-ex]].
59. Y. H. Lin, H. W. Hammer and U. G. Meißner, Eur. Phys. J. A **57**, no.8, 255 (2021) doi:10.1140/epja/s10050-021-00562-0 [arXiv:2106.06357 [hep-ph]].
60. J. C. Bernauer *et al.* [A1], Phys. Rev. C **90**, no.1, 015206 (2014) doi:10.1103/PhysRevC.90.015206 [arXiv:1307.6227 [nucl-ex]].
61. Y. H. Lin, H. W. Hammer and U. G. Meißner, Phys. Lett. B **816**, 136254 (2021) doi:10.1016/j.physletb.2021.136254 [arXiv:2102.11642 [hep-ph]].
62. S. K. Barcus, D. W. Higinbotham and R. E. McClellan, Phys. Rev. C **102**, no.1, 015205 (2020) doi:10.1103/PhysRevC.102.015205 [arXiv:1902.08185 [physics.data-an]].
63. J. Zhou, V. Khachatryan, H. Gao, S. Gorbaty and D. W. Higinbotham, Phys. Rev. C **106**, no.6, 065505 (2022) doi:10.1103/PhysRevC.106.065505 [arXiv:2110.02557 [hep-ph]].
64. Z. F. Cui, D. Binosi, C. D. Roberts and S. M. Schmidt, Chin. Phys. Lett. **38**, no.12, 121401 (2021) doi:10.1088/0256-307X/38/12/121401 [arXiv:2109.08768 [hep-ph]].
65. Y. Q. Ma and J. W. Qiu, Phys. Rev. D **98**, no.7, 074021 (2018) doi:10.1103/PhysRevD.98.074021 [arXiv:1404.6860 [hep-ph]].
66. B. U. Musch, P. Hagler, J. W. Negele and A. Schafer, Phys. Rev. D **83**, 094507 (2011) doi:10.1103/PhysRevD.83.094507 [arXiv:1011.1213 [hep-lat]].
67. T. Bhattacharya, V. Cirigliano, S. Cohen, R. Gupta, H. W. Lin and B. Yoon, Phys. Rev. D **94**, no.5, 054508 (2016) doi:10.1103/PhysRevD.94.054508 [arXiv:1606.07049 [hep-lat]].
68. D. Djukanovic, PoS **LATTICE2021**, 009 (2022) doi:10.22323/1.396.0009 [arXiv:2112.00128 [hep-lat]].
69. P. J. Mohr, D. B. Newell and B. N. Taylor, Rev. Mod. Phys. **88**, no.3, 035009 (2016) doi:10.1103/RevModPhys.88.035009 [arXiv:1507.07956 [physics.atom-ph]].
70. P. A. Zyla *et al.* [Particle Data Group], PTEP **2020**, no.8, 083C01 (2020) doi:10.1093/ptep/ptaa104
71. L. C. Maximon and J. A. Tjon, Phys. Rev. C **62**, 054320 (2000) doi:10.1103/PhysRevC.62.054320 [arXiv:nucl-th/0002058 [nucl-th]].
72. M. Vanderhaeghen, J. M. Friedrich, D. Lhuillier, D. Marchand, L. Van Hoorebeke and J. Van de Wiele, Phys. Rev. C **62**, 025501 (2000) doi:10.1103/PhysRevC.62.025501 [arXiv:hep-ph/0001100 [hep-ph]].
73. W. Xiong, JLAB-PHY-20-3266.
74. J. P. Karr, D. Marchand and E. Voutier, Nature Rev. Phys. **2**, no.11, 601-614 (2020) doi:10.1038/s42254-020-0229-x
75. R. Gilman *et al.* [MUSE], [arXiv:1709.09753 [physics.ins-det]].
76. E. Cline, J. Bernauer, E. J. Downie and R. Gilman, SciPost Phys. Proc. **5**, 023 (2021) doi:10.21468/SciPostPhysProc.5.023
77. A. Gasparian *et al.* [PRad], [arXiv:2009.10510 [nucl-ex]].
78. C. Dreisbach *et al.* [COMPASS++/AMBER working group], PoS **DIS2019**, 222 (2019) doi:10.22323/1.352.0222
79. C. Quintans [AMBER], Few Body Syst. **63**, no.4, 72 (2022) doi:10.1007/s00601-022-01769-7
80. S. Belostotski, N. Sagidova and A. Vorobyev, [arXiv:1903.04975 [hep-ph]].
81. A. Vorobyev, Phys. Part. Nucl. Lett. **16**, no.5, 524-529 (2019) doi:10.1134/S1547477119050303 [arXiv:1905.03181 [nucl-ex]].
82. T. Suda *et al.* J. Particle Accelerator Society of Japan **15** (2018) 52-59.
83. T. Suda, J. Phys. Conf. Ser. **2391**, no.1, 012004 (2022) doi:10.1088/1742-6596/2391/1/012004
84. O. Tomalak and M. Vanderhaeghen, Phys. Rev. D **93**, no.1, 013023 (2016) doi:10.1103/PhysRevD.93.013023 [arXiv:1508.03759 [hep-ph]].
85. J. Ahmed, P. G. Blunden and W. Melnitchouk, Phys. Rev. C **102**, no.4, 045205 (2020) doi:10.1103/PhysRevC.102.045205 [arXiv:2006.12543 [nucl-th]].
86. E. Cline, W. Lin, P. Roy, P. E. Reimer, K. E. Mesick, A. Akmal, A. Alie, H. Atac, A. Atencio and C. Ayerbe Gayoso, *et al.* Phys. Rev. C **105**, no.5, 055201 (2022) doi:10.1103/PhysRevC.105.055201 [arXiv:2109.09508 [physics.ins-det]].
87. A. Afanasev, J. Ahmed, I. Akushevich, J. C. Bernauer, P. G. Blunden, A. Bressan, D. Byer, E. Cline, M. Diefenthaler and J. M. Friedrich, *et al.* [arXiv:2012.09970 [nucl-th]].
88. A. Vorobyev and N. Sagidova, [arXiv:1912.06065 [physics.ins-det]].
89. F. Hug, K. Aulenbacher, S. Friederich, P. Heil, R. Heine, R. Kempf, C. Matejcek and D. Simon, doi:10.18429/JACoW-ERL2019-MOCXBS05
90. S. S. Caiazza, P. Achenbach, S. Aulenbacher, M. Biroth, M. Christmann, A. Denig, L. Doria, J. Geimer, P. Gülker and M. Littich, *et al.* J. Phys. Conf. Ser. **1498**, 012022 (2020) doi:10.1088/1742-6596/1498/1/012022
91. J. C. Bernauer, EPJ Web Conf. **234**, 01001 (2020) doi:10.1051/epjconf/202023401001